HYPERSPECTRAL NEUTRON CT WITH MATERIAL DECOMPOSITION

Thilo Balke[1,2]   *Alexander M. Long*[2]   *Sven C. Vogel*[2]   *Brendt Wohlberg*[2]   *Charles A. Bouman*[1]

[1]School of Electrical and Computer Engineering, Purdue University, West Lafayette, IN 47907, USA
[2]Los Alamos National Laboratory, Los Alamos, NM 87545, USA

ABSTRACT

Energy resolved neutron imaging (ERNI) is an advanced neutron radiography technique capable of non-destructively extracting spatial isotopic information within a given material. Energy-dependent radiography image sequences can be created by utilizing neutron time-of-flight techniques. In combination with uniquely characteristic isotopic neutron cross-section spectra, isotopic areal densities can be determined on a per-pixel basis, thus resulting in a set of areal density images for each isotope present in the sample. By preforming ERNI measurements over several rotational views, an isotope decomposed 3D computed tomograpy is possible.

We demonstrate a method involving a robust and automated background estimation based on a linear programming formulation. The extremely high noise due to low count measurements is overcome using a sparse coding approach. It allows for a significant computation time improvement, from weeks to a few hours compared to existing neutron evaluation tools, enabling at the present stage a semi-quantitative, user-friendly routine application.

Index Terms— neutron imaging, time-of-flight, neutron computed tomography, material decomposition

1. INTRODUCTION

Since neutrons interact with the nucleus, rather than the electron shell such as X-rays, protons, or electrons, neutron radiography can offer complementary information to more conventional radiography probes. With neutron radiography, distinctive attenuation cross-sections, that depend both on the isotopic compositions and incoming neutron energies, can result in contrast mechanisms and material penetrabilities that are fundamentally different from x-rays [1]. Moreover, with the advent of short-pulsed spallation neutron sources capable of producing intense and wide neutron spectra, and ultrafast, pixel dense neutron detectors coming to market [2, 3], neutron radiographs can be further resolved based on the energy of the incoming neutrons using neutron time-of-flight (TOF) techniques [4]. This advanced technique, known as energy resolved neutron imaging (ERNI), has been developed at several neutron facilities around the world, such as ISIS [5], LANSCE [6], and J-PARC [7], with broad appli-
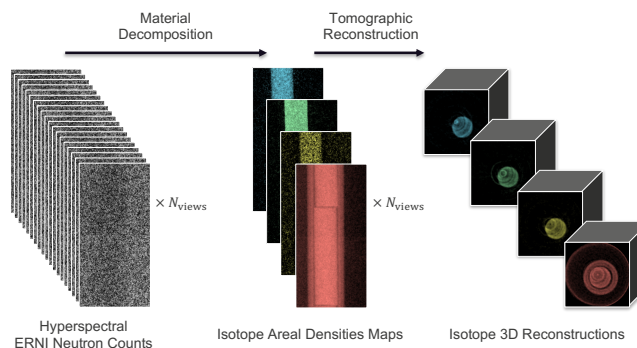
Fig. 1. From ERNI to material decomposed CT

cations ranging from nuclear fuel development [8] to gas pressure measurements [9] to 2D temperature mapping [10]. Of particular interest is the application of ERNI with epithermal neutrons, where many neutron absorption resonances are observed throughout the spectrum. The underlying isotopic areal densities can be measured by fitting known cross section spectra to the measured energy-dependent transmissions on a per-pixel basis. This technique allows for not only 2D spatial mapping of specific isotopic distributions, but also 3D reconstruction of the isotopic density distribution by performing ERNI measurements over many rotational views and subsequent computed tomograpy (CT) reconstruction. Compared to dual-energy CT [11] which uses two energies, in hyperspectral CT hundreds or thousands of energies can be leveraged to infer material quantities.

To date, the typical analysis process of ERNI measurements have proven to be cumbersome and computationally intensive, with the use of nuclear reaction codes, such as SAMMY [12]. With fitting routines taking seconds per transmission spectrum of a single pixel, analysis using SAMMY is computationally intensive and its application to large scale CT and radiography can require months, of computation time to render a single CT data set. Given these challenges, there is a great need for faster analysis tools that take advantage of state-of-the-art image enhancement techniques.

In this paper we present an efficient and comprehensive methodology to compute material decomposed radiographs and 3D reconstructions from ERNI radiography measurements (see Fig. 1). We demonstrate the method on real data acquired at Flight Path 5 of the 20 Hz spallation neutron

3482

source at LANSCE [6] of the Los Alamos National Laboratory. Reliable background correction is essential for accurate computation of the transmission spectra. Although explicit formulations of the background have been proposed [1], in practice this task is not performed in a standardized way [8]. We propose a robust, linear programming approach that is reproducible and scales computationally well with the size of the CT data set. The reconstruction of the material decomposed areal density maps is based upon a model-based iterative approach. Since ERNI measurements typically suffer from extremely poor statistics due to the flux limitations of even the world's most intense neutron sources, incorporating a Poisson counting model and Bayesian formulation in our approach helps overcome the severe noise.

2. RECONSTRUCTION MODEL

In this section, we derive the basic equations of the physical measurements taken in the hyperspectral tomographic system. In short, we first compute a material decomposition from the hyperspectral measurements and then compute individual, material decomposed volumetric CT reconstructions. This has the advantage of reducing the dimensionality in a meaningful way, while reducing the effects of noise.

2.1. Hyperspectral Model

Let $\alpha_{i,k}^o$ and $\alpha_{i,k}^b$ be the observed neutron counts of the object scan (with sample) and blank scan (without sample), respectively, at projection i and TOF bin (or energy bin) k. Then, it is assumed that the object and blank counts are given by

$$\alpha_{i,k}^o = \lambda_{i,k}^o + \beta_{i,k}^o \quad \text{and} \quad \alpha_{i,k}^b = \lambda_{i,k}^b + \beta_{i,k}^b , \quad (1)$$

where λ denotes signal counts and β the background counts whose estimation is described in section 2.4. With all these terms known, the attenuation, Y, is

$$Y_{i,k} = -\log\left(\frac{\lambda_{i,k}^o}{\lambda_{i,k}^b}\right) = -\log\left(\frac{\alpha_{i,k}^o - \beta_{i,k}^o}{\alpha_{i,k}^b - \beta_{i,k}^b}\right) , \quad (2)$$

where the transmission is referred to as

$$T_{i,k} = \frac{\alpha_{i,k}^o - \beta_{i,k}^o}{\alpha_{i,k}^b - \beta_{i,k}^b} . \quad (3)$$

Additionally, the transmission from (3) relates the attenuation density of the sample through Beer's law,

$$T_{i,k} = \exp(-\sum_j A_{i,j} U_{j,k} + B_{i,k}) , \quad (4)$$

where A is the system matrix modeling the tomographic projection, $A_{i,j}$ corresponds to i^{th} projection with the jth voxel, $U_{j,k}$ is the attenuation density of the jth voxel at the kth TOF bin, and B is a noise matrix capturing the modified counting noise. By equating (3) and (4) we can thus relate the measurements to the unknown and desired quantities, $U_{i,k}$,

$$Y = AU + B , \quad (5)$$

where Y is the matrix of energy-resolved attenuation measurements. B can be modeled as white Gaussian noise but to justify this consider again (2). As $\lambda_{i,k}$ and $\beta_{i,k}$ model independent counting events, we assume independent Poisson statistics. The variance of the attenuation, $Y_{i,k}$, given the attenuation density, U, is approximated as

$$\text{var}(Y_{i,k}|U) \approx \frac{\alpha_{i,k}^o + \beta_{i,k}^o}{(\alpha_{i,k}^o - \beta_{i,k}^o)^2} + \frac{\alpha_{i,k}^b + \beta_{i,k}^b}{(\alpha_{i,k}^b - \beta_{i,k}^b)^2} , \quad (6)$$

since for any differentiable function, f, and a random variable, X, $\text{var}(f(X)) \approx \text{var}(X)[\partial f(u)/\partial u]^2|_{u=X}$. Note that, as expected, the uncertainty of the attenuation explodes if the counts get dominated by background. Let V refer to the inverse variance in matrix form, where

$$V_{i,k} = 1/\text{var}(Y_{i,k}|U) \quad \text{and} \quad V_i = \text{diag}\{V_{i,*}\} \quad (7)$$

so that V_i is the inverse covariance matrix of the ith row of Y given U. Using this model, the conditional negative log-likelihood of the hyperspectral data, Y, can be derived to be

$$-\log p(Y|U) = \frac{1}{2}\sum_i \|Y_i - A_iU\|_{V_i}^2 = \frac{1}{2}\|Y - AU\|_{\odot V}^2 , \quad (8)$$

where we define the weighted norms $\|y\|_B^2 = \sum_{i,j} y_i \, B_{i,j} \, y_j$ for a vector, y, and $\|Y\|_{\odot B}^2 = \sum_{i,j} Y_{i,j}^2 B_{i,j}$ for a matrix, Y, and where $Y_i = Y_{i,*}$ is the ith row of Y and $A_i = A_{i,*}$ is the ith row of A.

2.2. Material Decomposed CT Model

Directly optimizing the negative log-likelihood of (8) is not very practical for several reasons. It is assumed that the number of energy bins, N_e, is very large (several thousands) and the measurements are very noisy, thus directly solving for the hyperspectral attenuation densities, U, would imply computing a separate noisy CT for each energy which would make each reconstruction virtually unusable. Instead, assuming only a small number of relevant isotopes, $N_m \ll N_e$, with distinct cross section spectra present, the dimensionality and noise properties can be drastically improved.

More specifically, we represent the unknown attenuation density, U, as a composition of materials using the model

$$U = XD , \quad (9)$$

where X is the $N_v \times N_m$ matrix representing the material decomposed reconstruction, N_v is the number of voxels, and D is the $N_m \times N_e$ dictionary of spectral responses (cross sections) for each isotope. Similarly, the attenuation measurements are modeled as a composition of materials

$$Y = ZD + B , \quad (10)$$

where $Z = AX$ is the $N_p \times N_m$ matrix of areal densities and N_p is the number of projections measured. Combining these equations, the forward model for our material decomposed

3483

tomographic data is given by

$$-\log p(Z|X) = \frac{1}{2}\sum_i \|Z_i - A_i X\|_{W_i}^2. \qquad (11)$$

In this case, the inverse covariance matrices, W_i, are not necessarily diagonal and can be approximated from the original covariance matrices, V_i,

$$W_i = \mathbb{E}\left[(BD^+)^\top (BD^+)\right] = (D^+)^\top V_i D^+ , \qquad (12)$$

where $D^+ = D^\top (DD^\top)^{-1}$ is $N_{\mathrm{e}} \times N_{\mathrm{m}}$ Moore–Penrose pseudo-inverse of D.

This new model has the immediate benefit of reduced dimensionality, but it retains the problem that the covariance matrices, W_i, are not necessarily diagonal, as opposed to the V_i's. However, in many cases the W_i matrices can be approximated as being diagonal if the dictionary entries of the cross section matrix, D, are approximately orthogonal. With this assumption, one can separate the weights into N_{m} diagonal matrices, $W^{(m)}$, where we define $(W^{(m)})_{i,i} = (W_i)_{m,m}$ such that we get N_{m} individual conventional CT problems

$$-\log p(Z|X) \approx \frac{1}{2}\sum_m \|Z^{(m)} - A X^{(m)}\|_{W^{(m)}}^2 , \qquad (13)$$

where $X^{(m)} = X_{*,m}$ and $Z^{(m)} = Z_{*,m}$ are the material decomposed reconstructions and sinograms, respectively. In this case, each material reconstruction, $X^{(m)}$, derived from material density map, $Z^{(m)}$, can be computed independently with the use of a CT reconstruction algorithm minimizing the log-likelihood of (13) for the unknown, $X^{(m)}$, in conjunction of an appropriate prior model.

The reconstruction follows a two step approach. In the first step the areal density maps, $\hat{Z}$, are estimated as described in section 2.3. In the second step the tomographic reconstruction is estimated using the likelihood model of (13) with the estimate, $\hat{Z}$, in the place of Z.

2.3. Material Decomposition of Neutron Attenuation

Before the tomographic reconstruction is performed, the material decomposed sinogram, $\hat{Z}$, is estimated from the hyperspectral attenuation measurements, Y, given by (10), $Y = ZD + B$. This quantity is estimated via a variant of Basis Pursuit Denoising (BPDN) [13]

$$\hat{Z} = \arg\min_{Z \geq 0} \left\{ \|D^\top Z^\top - Y^\top\|_{\odot V}^2 + \rho \|Z^\top\|_1 \right\} , \qquad (14)$$

where $\rho > 0$ is a regularization parameter that controls the strength of the ℓ_1 regularization term that promotes a sparse solution of low noise material maps. Note that this is a custom form of BPDN with an unconventional data weighting due to the fact that $(D^\top Z^\top - Y^\top)$ and V are matrices. The positivity constraint on the areal densities narrows down the search manifold to the non-negative quadrant. Since the cost function of (14) is separable across projections, the problem can be solved independently for each pixel.

Importantly, equation (14) dramatically reduces the di-
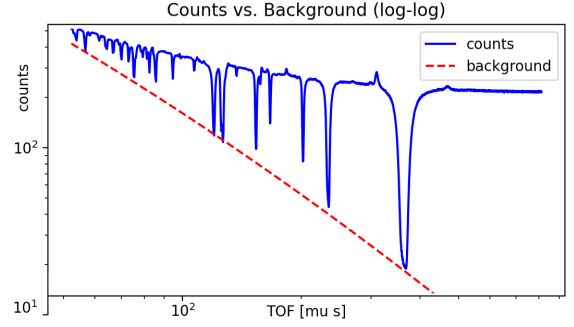
Fig. 2. Neutron counts over TOF with background estimate on a log-log scale. Sample is a 2.54 mm thick tantalum foil

mensionality of the problem. This is because the number of columns in Z is the number of materials, N_{m} (6 in our experiment), while the number of columns of Y is the number of TOF bins, N_{e} (2290 in our experiment).

2.4. Background Estimation

As (2) describes, the observed neutron counts, $\alpha_{i,k}$, are modeled as a sum of direct counts, $\lambda_{i,k}$, and background counts, $\beta_{i,k}$. Fig. 2 shows the neutron count spectrum with a tantalum foil sample. Due to the strong neutron absorption resonances of tantalum, deep dips in the spectrum are visible. For the deepest of those dips, the direct counts are assumed to be approximately zero. Further, when displayed in the log-log domain, as in this figure, it is assumed that the background is a smooth function within the energy region of interest. The background estimate is then intuitively the *highest, smooth, lower bound of the neutron counts*. We will first describe the background correction method for a single, low noise neutron spectrum and later illustrate how to deploy this method for high noise imaging applications.

More precisely, let $\alpha = [\alpha_{i,1}, ..., \alpha_{i,N_{\mathrm{e}}}]^\top$ and $\beta = [\beta_{i,1}, ..., \beta_{i,N_{\mathrm{e}}}]^\top$ be the vectors corresponding to the total and background counts, respectively, while $t = [t_{i,1}, ..., t_{i,N_{\mathrm{e}}}]^\top$ is the vector of corresponding TOF's. In the log-log domain, we define $\tilde{\alpha} = \log \alpha$, $\tilde{\beta} = \log \beta$, and $\tilde{t} = \log t$. The background, $\tilde{\beta}$, is a smooth function and thus we are choosing a polynomial of low degree as a functional

$$\tilde{\beta} = \sum_n \tilde{t}^n x_n = G(\tilde{t}) x , \qquad (15)$$

where $x = [x_0, x_1, ...]^\top$ are the polynomial coefficients and Ax is the matrix formulation. To express the area under the curve in a similar way we have

$$\int_{\tilde{t}_1}^{\tilde{t}_N} G(\tilde{t}) x \, d\tilde{t} = \sum_n x_n \frac{\tilde{t}_N^{i+1} - \tilde{t}_1^{i+1}}{i+1} = -c^\top x . \qquad (16)$$

Written this way it matches the linear programming form,

$$\hat{x} = \arg\min_{x,\, G(\tilde{t})x \leq \tilde{\alpha}} \left\{ c^\top x \right\} , \qquad (17)$$

where the solution for the background is $\beta = \exp(G(\tilde{t})\hat{x})$.

This method solves the background estimation for a single, low noise spectrum, however, to work by itself for the whole 2D radiograph the count measurements in a TOF neutron imaging facility are usually too noisy and possibly lack the presence of totally opaque resonances. Thus, for the 2D radiographs it is assumed that a single background estimate, β^* can be obtained from a reference measurement, α^*, or reference region and that the background for individual projections, i, is proportional to the reference background

$$\beta_{i,*} = r_i \beta^* \quad \text{and} \quad r_i = \frac{\sum_{k \in \Omega} \alpha_{i,k}}{\sum_{k \in \Omega} \alpha_k^*} . \tag{18}$$

The scale factor, r_i, is computed as the ratio of neutron counts in TOF regions, Ω, that are assumed to be transparent to neutrons and the low noise α^* and β^* are the reference total counts and background counts, respectively.

3. EXPERIMENTAL RESULTS

To demonstrate our approach we use ERNI measurements from LANSCE's [6] neutron source, a neutron sensitive MCP detector [2], in conjunction with four Timepix readout chips with 55×55 μm^2 pitch [3]. For the CT measurement with 100 views, 2290 TOF bins each with a bin width of 320 ns was used over an energy range of approximately 1 eV to 60 keV. The sample consists of UPuZr transmutation fuel slugs, in a double-walled cylindrical steel container, with resonant isotopes in that energy region assumed to be ^{237}Np, ^{238}U, ^{239}Pu, ^{240}Pu, ^{241}Am; and a ^{1}H isotope placeholder capturing all non-resonant isotopes that might be present (e.g. Zr). The material decomposition of (14), reconstructed areal density maps, $\hat{Z}$, of a single view are shown in Fig. 3. The BPDN problem is optimized using an ADMM [14] formulation and the SPORCO [15] Python package.
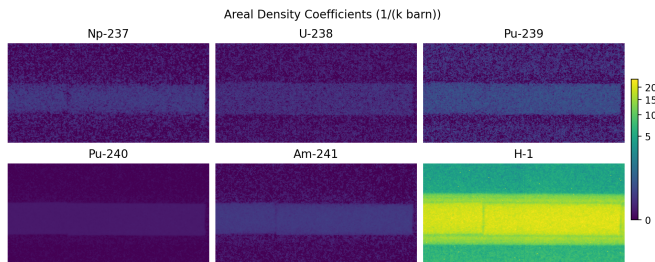
Fig. 3. Areal density maps (Z) of a single radiograph

The fast, model-based parallel beam reconstruction software, SVMBIR [16] was used for the CT reconstruction, optimizing the log-likelihood from (13) with a q-GGMRF prior model serving as regularization term [17] for each isotope independently as in (13). In addition, an average attenuation sinogram can by computed by averaging Y across the energies. The CT reconstruction (axial slices) for the average attenuation, the non-resonant group, and for the ^{241}Am isotope

Fig. 4. Material decomposed CT Reconstruction (X)

Table 1. Computation time comparison of the material decomposition. (*: interpolated, **: extrapolated)

Compuation Time	SAMMY [12]	Proposed
Time per pixel spectrum	1.72 s	2.18 ms*
Time per CT data set	248.8 days**	7.58 h

are shown in Fig. 4. With this reconstruction, it is clearly visible that both the fuel core and the steel container contain non-resonant isotopes, presumably Zr and Fe, whereas the ^{241}Am only shows up in the center of the fuel slug. Also, as a void in the 7 o'clock segment off the center shows up in all isotope maps, it can be assumed that this is a void.

The computation time is dominated by the material decomposition from (14) and for the data set consisting of $504 \times 248 \times 2290 \times 100$ data points (pixel, pixel, TOF bins, view angles) only approximately 7.58 hours on a 8-core 2.4 GHz machine was required. We estimate (by extrapolating from a single-spectrum analysis) that it would have taken approximately 8.3 months to solve the same problem using SAMMY (see Tab. 1). The estimated densities from a single low noise

Table 2. Estimated Areal densities for a single spectrum in [atoms / 1000 barn]. (* SAMMY did not converge using ^{1}H)

Areal Densities	SAMMY [12]	Proposed
^{237}Np	0.471	0.577
^{238}U	10.665	1.163
^{239}Pu	1.930	2.284
^{240}Pu	0.540	0.001
^{241}Am	0.493	0.727
^{1}H equivalent	N/A*	0.031

spectrum are shown in Tab. 2. Although most isotopes have been estimated relatively similar to the SAMMY benchmark, both ^{238}U and ^{240}Pu show large deviations. This is attributed to the fact that those isotopes show very few but very intense resonances which cause the signal to reach into the noise floor. Thus, to call the proposed tool truly quantitative, an extensive comparison and evaluation is necessary, however we believe that the so far extreme speed benefits are providing a very promising tool for qualitative analysis with possibly future quantitative verification.

3485

4. REFERENCES

[1] P. Schillebeeckx, B. Becker, Y. Danon, K. Guber, H. Harada, J. Heyse, A. R. Junghans, S. Kopecky, C. Massimi, M. C. Moxon, N. Otuka, I. Sirakov, and K. Volev, "Determination of resonance parameters and their covariances from neutron induced reaction cross section data," *Nuclear Data Sheets*, vol. 113, no. 12, pp. 3054–3100, 2012.

[2] A. S. Tremsin, J. B. McPhate, J. V. Vallerga, O. H. W. Siegmund, J. S. Hull, W. B. Feller, and E. Lehmann, "Detection efficiency, spatial and timing resolution of thermal and cold neutron counting MCP detectors," *Nuclear Instruments and Methods in Physics Research Section A: Accelerators, Spectrometers, Detectors and Associated Equipment*, vol. 604, no. 1-2, pp. 140–143, 2009.

[3] A. S. Tremsin, J. B. McPhate, J. V. Vallerga, O. H. W. Siegmund, W. B. Feller, E. Lehmann, and M. Dawson, "Improved efficiency of high resolution thermal and cold neutron imaging," *Nuclear Instruments and Methods in Physics Research Section A: Accelerators, Spectrometers, Detectors and Associated Equipment*, vol. 628, no. 1, pp. 415 – 418, 2011, VCI 2010.

[4] E. H. Lehmann, G. Frei, P. Vontobel, L. Josic, N. Kardjilov, A. Hilger, W. Kockelmann, and A. Steuwer, "The energy-selective option in neutron imaging," *Nuclear Instruments and Methods in Physics Research Section A: Accelerators, Spectrometers, Detectors and Associated Equipment*, vol. 603, no. 3, pp. 429 – 438, 2009.

[5] J. W. G. Thomason, "The ISIS spallation neutron and muon source—the first thirty-three years," *Nuclear Instruments and Methods in Physics Research Section A: Accelerators, Spectrometers, Detectors and Associated Equipment*, vol. 917, pp. 61–67, 2019.

[6] P. W. Lisowski and K. F. Schoenberg, "The Los Alamos neutron science center," *Nuclear Instruments and Methods in Physics Research Section A: Accelerators, Spectrometers, Detectors and Associated Equipment*, vol. 562, no. 2, pp. 910–914, 2006.

[7] Y. Ikeda, "Current status of 1 MW pulse spallation neutron source (JSNS) of J-PARC," *Journal of nuclear materials*, vol. 343, no. 1-3, pp. 7–13, 2005.

[8] A. S. Tremsin, S. C. Vogel, M. Mocko, M. A. M. Bourke, V. Yuan, R. O. Nelson, D. W. Brown, and W. B. Feller, "Non-destructive studies of fuel pellets by neutron resonance absorption radiography and thermal neutron radiography," *Journal of Nuclear Materials*, vol. 440, no. 1-3, pp. 633–646, 2013.

[9] A. S. Tremsin, A. S. Losko, S. C. Vogel, D. D. Byler, K. J. McClellan, M. A. M. Bourke, and J. V. Vallerga, "Non-contact measurement of partial gas pressure and distribution of elemental composition using energy-resolved neutron imaging," *AIP Advances*, vol. 7, no. 1, pp. 015315, 2017.

[10] A. S. Tremsin, W. Kockelmann, D. E. Pooley, and W. B. Feller, "Spatially resolved remote measurement of temperature by neutron resonance absorption," *Nuclear Instruments and Methods in Physics Research Section A: Accelerators, Spectrometers, Detectors and Associated Equipment*, vol. 803, pp. 15–23, 2015.

[11] X. Liu, L. Yu, A. N. Primak, and C. H. McCollough, "Quantitative imaging of element composition and mass fraction using dual-energy CT: Three-material decomposition," *Medical physics*, vol. 36, no. 5, pp. 1602–1609, 2009.

[12] N. M. Larson, "Updated users' guide for SAMMY multilevel R-matrix fits to neutron data using Bayes' equation," Tech. Rep., Oak Ridge National Lab., TN (US), 2008, https://www.ornl.gov/onramp/sammy.

[13] S. Chen and D. Donoho, "Basis pursuit," in *Proceedings of 1994 28th Asilomar Conference on Signals, Systems and Computers*, 1994, vol. 1, pp. 41–44 vol.1.

[14] S. Boyd, N. Parikh, and E. Chu, *Distributed optimization and statistical learning via the alternating direction method of multipliers*, Now Publishers Inc, 2011.

[15] B. Wohlberg, "SPORCO: A Python package for standard and convolutional sparse representations," in *Proceedings of the 16th Python in Science Conference*, Katy Huff, David Lippa, Dillon Niederhut, and M Pacer, Eds., 2017, pp. 1 – 8, https://sporco.readthedocs.io/en/latest/.

[16] X. Wang, A. Sabne, S. Kisner, A. Raghunathan, C. Bouman, and S. Midkiff, "High performance model based image reconstruction," *SIGPLAN Not.*, vol. 51, no. 8, Feb. 2016, https://svmbir.readthedocs.io/en/latest/index.html.

[17] S. J. Kisner, E. Haneda, C. A. Bouman, S. Skatter, M. Kourinny, and S. Bedford, "Model-based CT reconstruction from sparse views," in *Second International Conference on Image Formation in X-Ray Computed Tomography*, 2012, pp. 444–447.